



Multivariate analysis-based laser-induced breakdown spectroscopy for monitoring of laser paint cleaning

Soojin Choi¹ · Jiyeon Choi¹ · Changkyoo Park²

Received: 8 September 2022 / Accepted: 18 November 2022 / Published online: 9 December 2022
© The Author(s), under exclusive licence to Springer-Verlag GmbH Germany, part of Springer Nature 2022

Abstract

In this study, a high-power Nd:YAG laser was used to remove a thick paint coating layer from 304L stainless steel (SS304L). Different numbers of laser paint cleaning processes were performed, and an electron probe micro analyzer (EPMA) analysis was used to examine the SS304L surface condition. The surface elemental distributions of SS304L were strongly dependent on the laser paint cleaning process owing to the different levels of paint removal. Laser-induced breakdown spectroscopy (LIBS) was also adopted to monitor the laser paint cleaning process. Two different types of LIBS-based 2-dimension (2D) mapping were developed. 2D elemental distribution maps were constructed using the LIBS peak intensities of Fe (374.95 nm) Cr (520.84 nm), and Na (588.99 nm). Moreover, 2D correlation coefficient distribution maps were constructed using the Pearson's correlation coefficient. These two different 2D mappings were compared with the elemental distribution maps obtained from the EPMA analysis, and the latter shows excellent agreement with the EPMA analysis. This study presents the possibility of the LIBS-based monitoring for the laser paint-cleaning process using multivariate correlation analysis.

1 Introduction

304L stainless steel (SS304L) is an austenitic stainless steel that contains both 18–20% chromium and 8–10.5% nickel, and this composition prevents the steel from corrosion. SS304L has good formability and machinability as well as excellent corrosion resistance and mechanical strength. Therefore, it has been extensively used in multiple industrial applications, such as heat exchangers, food and chemical containers, pressure vessels, nuclear power plants, automobiles, and ship buildings [1–7]. Protective surface coatings have been employed in stainless steels that are introduced in highly damaging and corrosive environments. To prevent unwanted damage and corrosion, the protective surface coating should be regularly maintained by coating removal and re-coating. Traditional abrasive blasting and chemical etching techniques have been widely adopted for maintenance

[8–11]. However, these conventional techniques can generate severe environmental and health issues owing to the use of airborne abrasive materials and strong acidic solutions. From this point of view, the laser cleaning technique has been considered as a promising maintenance method owing to its eco- and worker-friendly operation [12–14].

In the laser cleaning process, various monitoring techniques have been utilized for process optimization, residual contaminant measurement, and over-cleaning prevention. Micro-computed tomography (μ -CT) and micro-X-ray fluorescence spectroscopy (μ -XRF) techniques have been applied to evaluate the efficiency of laser cleaning of limestone monuments [15]. Optical coherence tomography (OCT) and reflection Fourier-transform infrared (FT-IR) spectroscopy were adopted to optimize the operative parameters for laser cleaning of historical easel paintings [16]. Field emission scanning electron microscopy (FE-SEM), electron probe microanalysis (EPMA), atomic force microscopy, and energy dispersive spectroscopy have been used to examine the laser cleaning of natural marine biofouling from the surface of aluminum alloys [17]. Moreover, acoustic techniques have also been considered for monitoring the laser cleaning process [18–21]. Tservelakis et al. [18] examined the laser cleaning effectiveness and potential damage to a marble slab via photoacoustic monitoring. Xiea et al. [19] and Zou et al. [21] used acoustic signals

✉ Changkyoo Park
ck0421@seoultech.ac.kr

¹ Department of Laser and Electron Beam Technologies, Korea Institute of Machinery and Materials, Daejeon 34103, Republic of Korea

² Department of Materials Science and Engineering, Seoul National University of Science and Technology, 01811 Seoul, Republic of Korea

Table 1 Chemical composition of 304L stainless steel

Elements	C	Si	Mn	P	S	Cr	Ni	Cu	Mo	Fe
wt%	0.021	0.386	1.462	0.031	0.002	18.137	8.064	0.216	0.112	Bal.

to monitor rust and paint removal through laser cleaning, respectively.

Laser-induced breakdown spectroscopy (LIBS) is a rapid and versatile surface chemical analysis technology that uses laser-induced plasmas. LIBS is a promising analytical technique for the in-line monitoring process because it provides information such as process quality and chemical composition without any sample pretreatment. Therefore, LIBS has been utilized to monitor the laser cleaning process of artworks, historic artifacts, and metal alloys [22–32]. Colao et al. [22] adopted LIBS as a monitoring tool for laser cleaning of the restoration of ancient marbles. Staicu et al. [23] and Scholten et al. [24] controlled the laser cleaning process using LIBS for painting restorations. Kono et al. [28] introduced feedback control for laser cleaning of fragile heritages (e.g., gold braids) to prevent unwanted damage. Li et al. [31] employed real-time LIBS monitoring for the laser cleaning of hot-rolled stainless steel. Mateo et al. [32] used LIBS to examine the chemical composition and thickness of protective paint layer for vessels. However, to the best of our knowledge, previous LIBS-based laser cleaning monitoring has been adopted for relatively low laser power applications, including artwork and heritage restorations. In addition, previous studies conducted the LIBS-based monitoring in a limited area (i.e., point-based analysis).

In this study, a 1.2 kW Q-switched Nd:YAG laser was employed to remove a thick protective coating (i.e., paint layer) from SS304L. The LIBS-based monitoring was used to examine the paint layer (or residue) on the SS304L substrate after the laser cleaning process. The 2-dimension (2D) mapping of the SS304L surface was performed using the LIBS peak intensities of Fe, Cr, and Na. Moreover, multivariate analysis of the LIBS spectra was conducted. The Pearson's correlation coefficients (Pearson's R) were calculated by comparing the LIBS spectra between the base metal (BM) and laser-cleaned specimens and were used to build the 2D correlation coefficient mapping of the SS304L surface. Then, two different types of 2D mappings were compared with the elemental distribution map obtained from the EPMA analysis (Figure S1). The 2D coefficient mapping with multivariate correlation analysis of the LIBS spectrum was first achieved for the laser cleaning process, and this study verified the capability of LIBS as an in-line monitoring tool for the high-power laser paint cleaning (LPC) process.

2 Materials and methods

2.1 Materials and experimental setup for LSC

In this study, a commercial SS304L (POSCO) with dimensions of 100 (W) × 100 (D) × 10 (H) mm³ was employed; its chemical composition is listed in Table 1. The as-received SS304L specimens were annealed at 1050 °C for 1 h in an Ar atmosphere, and then furnace-cooled to 25 °C [33]. Then, the specimens were polished using SiC paper with grit sizes of 180–4000. A painted SS304L specimen was prepared by applying a red epoxy paint (Korepox EH2350PTA, KCC) using a paint spray gun, and the thickness of the paint layer was approximately 320 μm. A 1.2 kW Q-switched Nd:YAG (Rigel i1200, Powerlase) with a pulse duration of 89 ns and central wavelength of 1064 nm was adopted for the laser paint cleaning (LPC) process. A laser power of 850 W was employed with a pulse frequency of 8 kHz, corresponding to a laser energy density of 1.64 J/cm². The laser energy density was obtained using the following equation:

$$\text{Laser energy density (J/cm}^2\text{)} = \frac{\text{Laser power (W)}}{\text{Repetition rate (Hz)} \times \text{Laser beam area (cm}^2\text{)}} \quad (1)$$

A laser beam size was 2.1 mm with a super-Gaussian energy distribution. The laser beam quality factors were 29.7 and 30.2 in the horizontal *x*-direction and vertical *y*-direction, respectively. The hatch distance and scan speed were set to 1.8 mm and 4 m/s, respectively. The laser beam was scanned using a two-dimensional galvanometer scanner (SUPERSCAN IIE-30, Raylase). The dimensions of LPC area were set to 40 × 40 mm², and the location of LPC was shifted by 0.6 mm for two subsequent LPC processes. Consequently, the final laser-cleaned area was 40 × 41.2 mm² (Fig. 1a). This LPC process was repeated twice (LPC 2), six times (LPC 6), and nine times (LPC 9). Figure 1b shows an image of the base metal, painted, and laser-paint-cleaned specimens.

2.2 Microstructure

The painted specimen and laser-paint-cleaned specimens were cut and polished with a low-speed cutting wheel and SiC paper, respectively. Then, the cross-sectional optical microscopy (OM) images were obtained before and after the

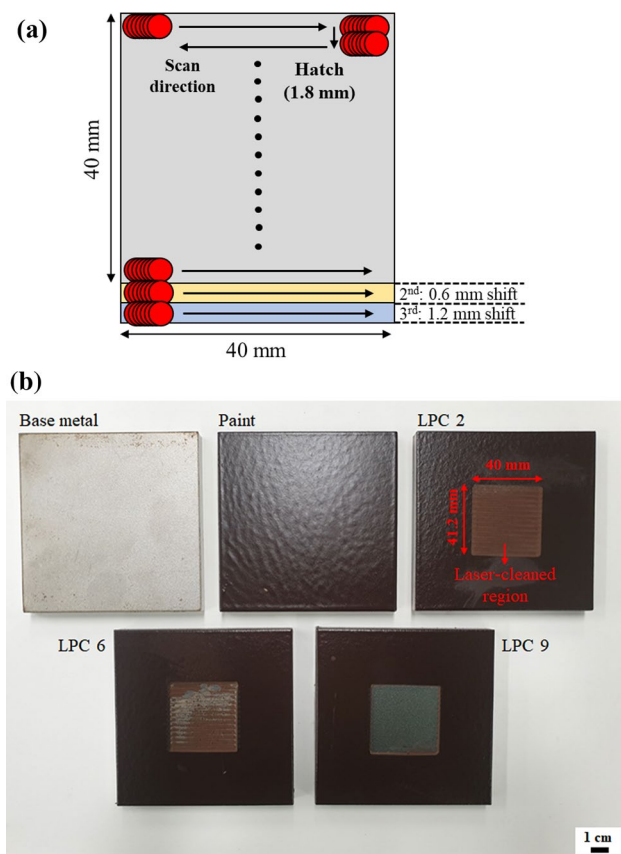


Fig. 1 a Schematic illustration of the laser paint cleaning process. b Image of the base metal, painted, and laser paint-cleaned specimens

LPC process. The EPMA analysis (EPMA-1610, Shimadzu) was performed to examine the laser paint removal after the LPC process. The top-sectional elemental distribution maps were examined with dimensions of $2 \times 2 \text{ mm}^2$ at the center of the laser-cleaned region.

2.3 Laser-induced breakdown spectroscopy

The LIBS analysis was followed by the EPMA analysis, and both analyses regions were identical. The experimental setup for the LIBS analysis is shown in Figure S2. A Q-switched Nd:YAG laser (VIRON, Quantel Laser) with a central wavelength of 1064 nm and a pulse duration of 7 ns was employed for the LIBS-based LPC monitoring. A laser pulse energy of 5 mJ was used with a pulse frequency of 1 Hz. The laser beam was focused on the specimen surface by plano-convex lens with a focal length of 50 mm. A spectrometer (IsoPlane 320, Princeton Instruments) coupled with an intensified charge-coupled device camera (PI MAX 4, Princeton Instruments) was employed for the acquisition of the laser-induced plasma. Plasma emission light was passed to the spectrometer through a plano-convex lens with a focal

length of 100 mm and a fiber optic cable with a core size of 600 μm . The spectral range was 370–630 nm, and the plasma signals were dispersed by a 150 g/mm grating. Moreover, the delay time and gate width were 1 and 5 μs , respectively. The specimens were moved using an x - and y -axis motorized stage (Figure S2a), and the LIBS spectra were acquired with a step size of 100 μm and dimensions of $2 \times 2 \text{ mm}^2$. Consequently, four hundred LIBS spectra were obtained for each specimen (Figure S2b).

2.4 Multivariate analysis

Multivariate correlation analysis of the LIBS spectrum was conducted by calculating the Pearson's coefficient, which can quantify the similarity of the LIBS spectra between the base metal and laser paint-cleaned specimens. The Pearson's coefficient can be obtained by dividing the covariance of two variables by the product of their standard deviation using the following equation:

$$\text{Pearson's coefficient} = \frac{\sum_{i=1}^n (x_i - \bar{x})(y_i - \bar{y})}{\sqrt{\sum_{i=1}^n (x_i - \bar{x})^2} \sqrt{\sum_{i=1}^n (y_i - \bar{y})^2}} \quad (2)$$

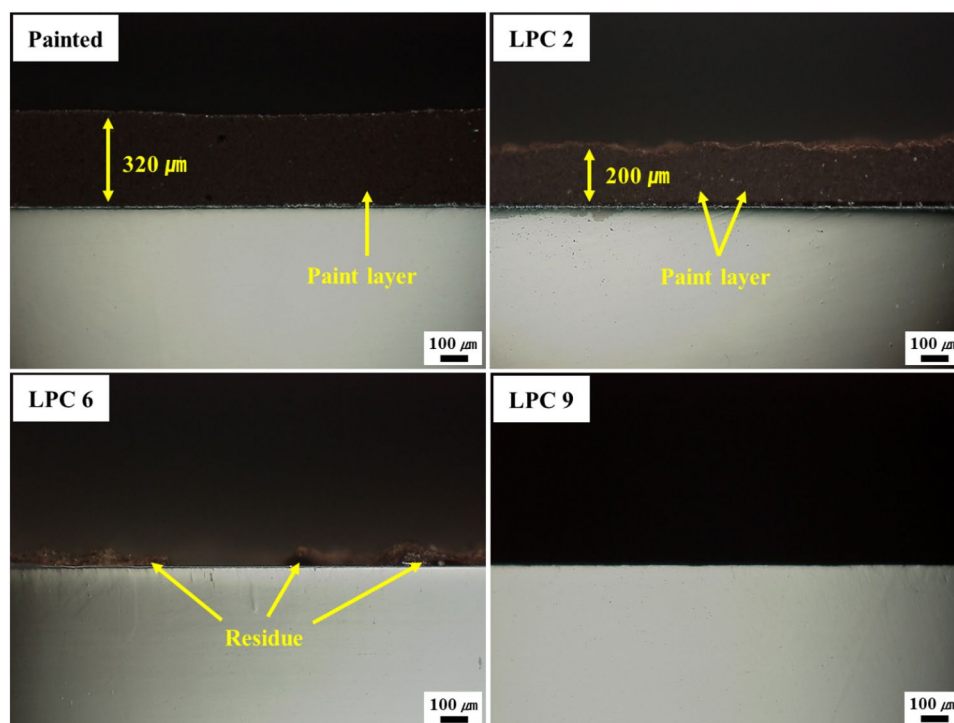
Here, x and y represent the signal intensities obtained from the LIBS spectra of the base metal and paint or laser-cleaned specimens, respectively. \bar{x} and \bar{y} are the average signal intensity values of x and y . Moreover, n represents the number of data points from each LIBS spectrum, and each LIBS spectrum is consisted of 1024 data points. The Pearson's coefficient ranges from -1 to 1. With the successful LPC process, the LIBS spectra of the laser-cleaned specimens are similar to those of the BM, and the Pearson's coefficient converges to 1. Python software was used to calculate the Pearson's coefficient.

3 Results and discussion

3.1 LPC process

Figure 2 shows the cross-sectional OM images before and after the LPC process. A paint layer with a thickness of approximately 320 μm was detected for the painted specimen (paint). After two repetitions of the LPC process (i.e., LPC 2), the paint layer still existed, while the thickness decreased to 200 μm owing to the laser paint removal. For the LPC 6, the paint layer was removed and an uneven surface was observed with the existing paint residues. In contrast, no paint layer or residues were detected at the surface of the LPC 9, indicating that the paint was completely removed by the LPC process.

Fig. 2 Cross-sectional OM images of the paint, LPC 2, LPC 6, LPC 9, and LPC 12



The EPMA analysis was performed to characterize the paint removal after the LPC process. Figure 3 shows the top-sectional backscattered electron (BSE) image and the corresponding elemental distribution maps of C, Fe, and Cr for the BM, paint, LPC 2, LPC 6, and LPC 9. A relatively homogenous elemental distribution with a high concentration of Fe and a low concentration of C was observed in the BM (Fig. 3a). In contrast, for the paint (Fig. 3b), a relatively high concentration of C was detected with a homogeneous elemental distribution. Moreover, a relatively low concentration of Fe was observed owing to the presence of an epoxy-based paint layer at the surface. For the LPC 2 (Fig. 3c), a low concentration of Fe and a high concentration of C were still observed even after two repetitions of the LPC process, indicating the presence of a paint layer at the surface. For the LPC 6 (Fig. 3d), high elemental segregation was analyzed. This is because the thick paint layer was removed, while the paint residues still existed at the surface even after six repetitions of the LPC process. Therefore, a high C distribution was observed at the paint residues, whereas a low C distribution was detected at the paint-free surface. In contrast, LPC 9 (Fig. 3e) shows a homogenous elemental distribution with a high concentration of Fe and a low concentration of C, suggesting that the paint layer was effectively removed by the LPC process.

3.2 LIBS-based 2D elemental mapping

Figure 4 shows the LIBS spectra of the BM, paint, and laser-cleaned specimens. The LIBS spectra were obtained using average values of four hundred spectra for each specimen. The main elements of SS304L are Fe and Cr, therefore the Fe and Cr peaks were observed at 374.95 and 520.84 nm for the BM. For the paint and laser-cleaned specimens, a distinct Na peak was detected at 588.99 nm due to the presence of Na element in the epoxy paint.

Figure 5 shows the magnified LIBS spectra for the Fe, Cr, and Na emission lines (marked with black arrows) with background subtraction. The background signal of the LIBS spectra is strongly dependent on the surface conditions, laser parameters, and experimental environments [34–37]. Therefore, the background subtraction was performed by setting the minimum LIBS signal intensity as the baseline. For the Fe and Cr peaks in Fig. 5a, b, respectively, the signal intensity of the peaks increased with an increase in the number of LPC processes. In contrast, the signal intensity of the Na peak (Fig. 5c) decreased as the number of LPC processes increased. This result indicates that the Fe, Cr, and Na peaks can be adopted to examine the laser paint cleaning level.

The Fe, Cr, and Na peaks in the LIBS spectrum were quantified and used to construct the LIBS-based 2D elemental mapping for comparison with that of the EPMA analysis. In this study, four hundred LIBS spectra were investigated to build a 2D mapping. Moreover, the peak intensity was calculated by integrating the area below each peak instead

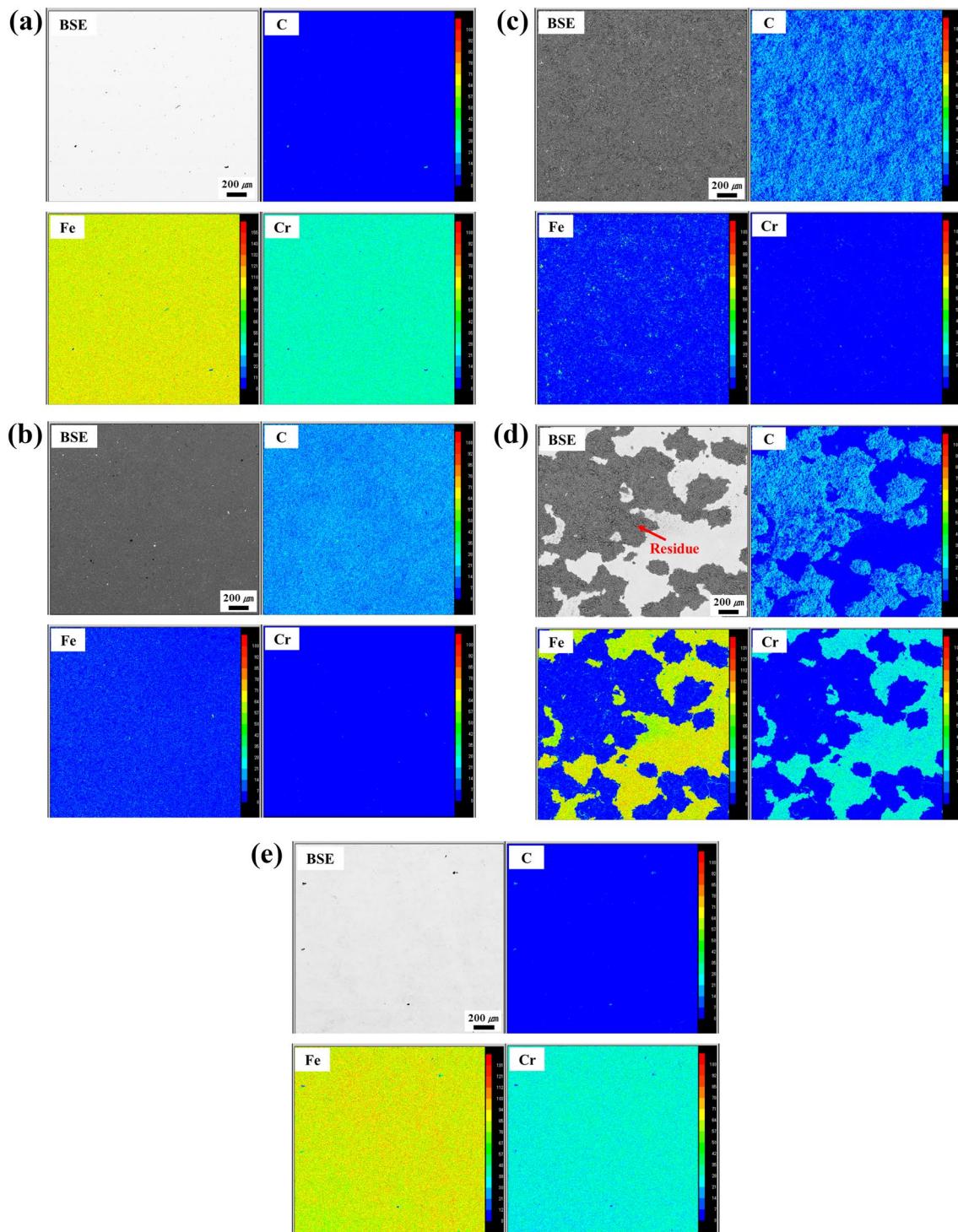


Fig. 3 BSE images and the corresponding elemental distribution maps obtained from the EMPA analysis for the **a** base metal, **b** paint, **c** LPC 2, **d** LPC 6, and **e** LPC 9

of taking the maximum values. This is because the peak shift can occur owing to a limitation of the spectroscopy resolution, resulting in a lower accuracy of the analysis [38]. The peak signal intensity could be varied even with a peak shift

of 0.5 nm. In contrast, the peak area-based analysis considers a relatively wide range of wavelengths (i.e., approximately 1–4 nm), thereby minimizing the influence of the peak shift. The peak area was measured in the wavelength

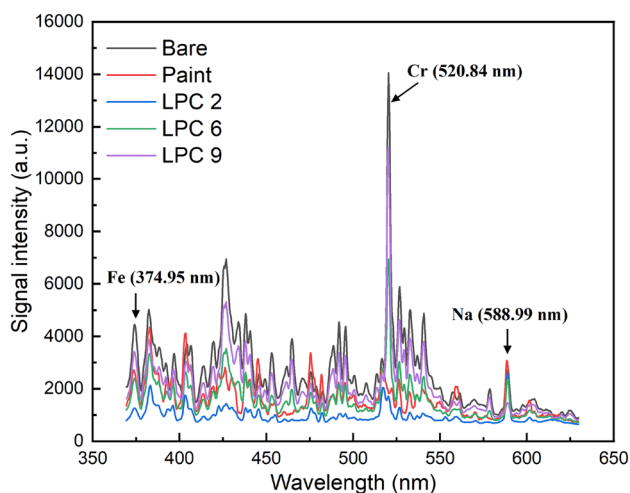


Fig. 4 LIBS spectra of the base metal, painted, LPC 2, LPC 6, and LPC 9 specimens

range of 372.18–375.45, 519.9–520.9, and 586.6–591.27 nm for the Fe, Cr, and Na elements, respectively. Peak area measurements were conducted using the Origin software (OriginLab).

Figure 6 shows the LIBS-based 2D elemental distribution maps of Fe, Cr, and Na for the BM and laser-cleaned specimens. In the case of the LPC 6 (Fig. 6c), the LIBS-based mapping of Fe, Cr, and Na showed elemental distributions similar to those of the EPMA analysis. Relatively low Fe and Cr concentrations (blue color) and a relatively high Na concentration (red color) were detected in the region of the paint residue. This result is equivalent to the EPMA analysis. However, in the case of the BM (Fig. 6a), LPC 2 (Fig. 6b), and LPC 9 (Fig. 6d), the LIBS-based elemental distribution maps show a low coincidence with those of the EPMA analysis. For every element, strong elemental segregations were observed in the limited region for the LIBS-based 2D mapping, whereas relatively uniform elemental distributions were observed in the EPMA analysis. The low coincidence in the elemental distribution maps between the LIBS-based 2D mapping and EPMA analysis was attributed to the non-uniformity of the plasma. When laser pulses for the LIBS analysis are applied to the specimens, a non-uniformity of plasma is generated, inducing a variation in signal intensity in the LIBS spectrum. The plasma-induced signal intensity variation becomes critical when the surface exhibits a relatively uniform elemental distribution. This is because, for a uniform surface, comparable LIBS spectra will be obtained at every location of the surface, and the plasma-induced signal intensity variation will be presented as elemental segregation in the 2D elemental maps, as shown in the BM, LPC 2, and LPC 9. In addition, no distinct differences were observed in the 2D elemental maps with or without the paint layer. The LPC 2 with a 200 μm thickness of paint layer and

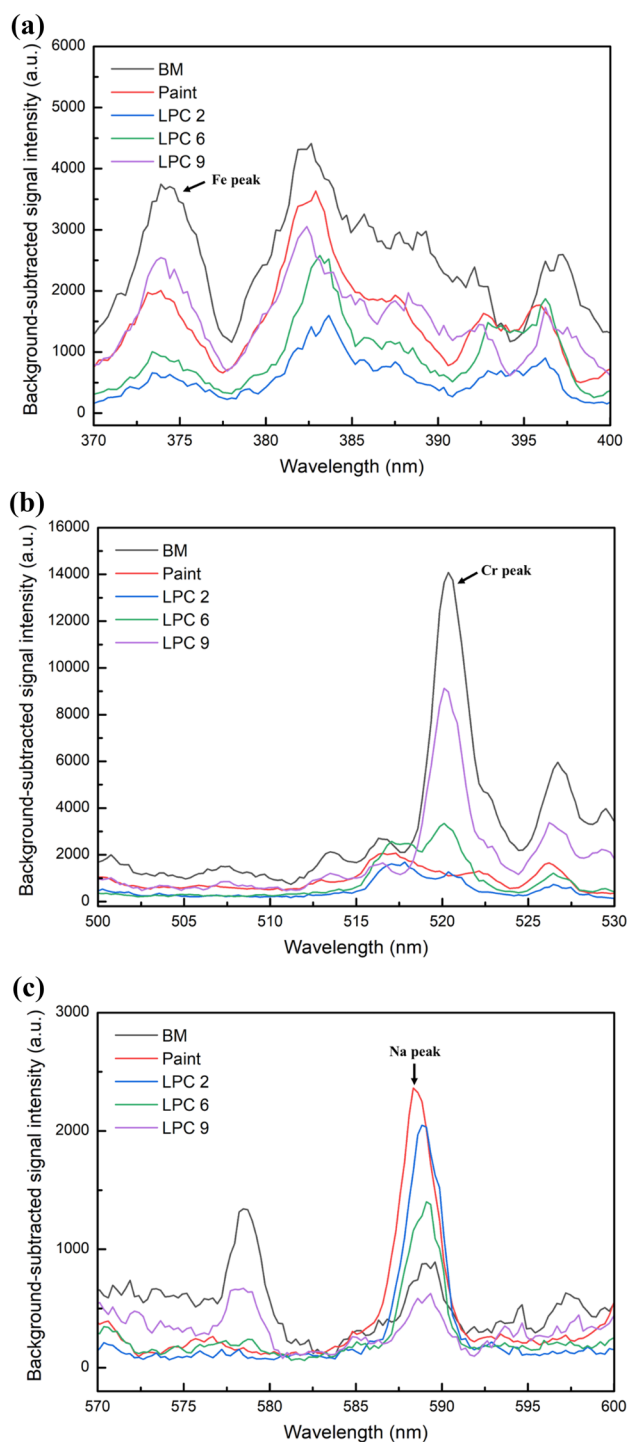


Fig. 5 Magnified LIBS spectra of the base metal, paint, LPC 2, LPC 6, and LPC 9 for the **a** Fe, **b** Cr, and **c** Na emission lines

the LPC 9 with no paint layer showed similar LIBS-based 2D elemental distribution maps. In other words, the LIBS-based 2D elemental distribution mapping has a relatively low accuracy for the BM, LPC 2, and LPC 9, which have relatively uniform surface elemental distributions compared

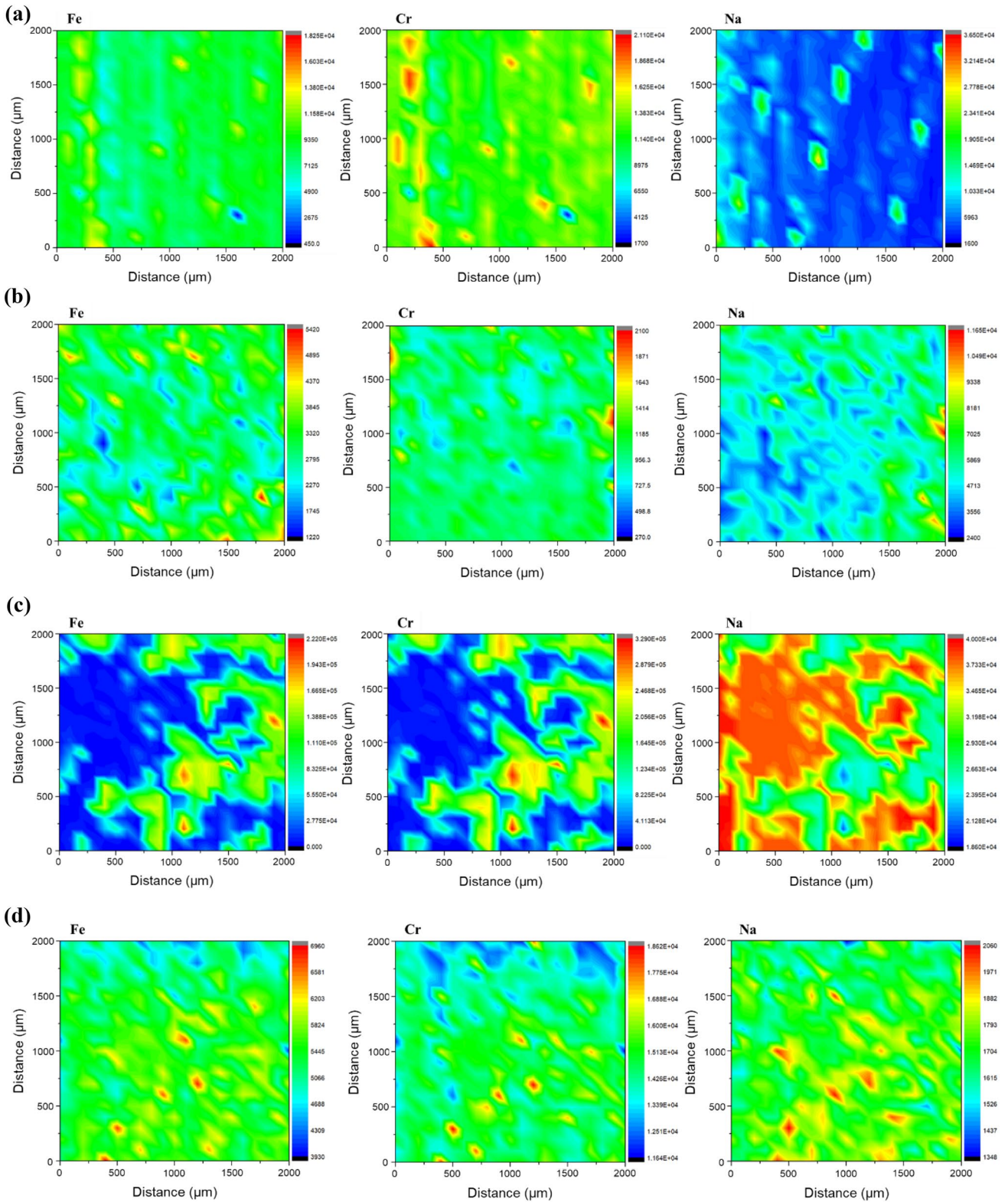
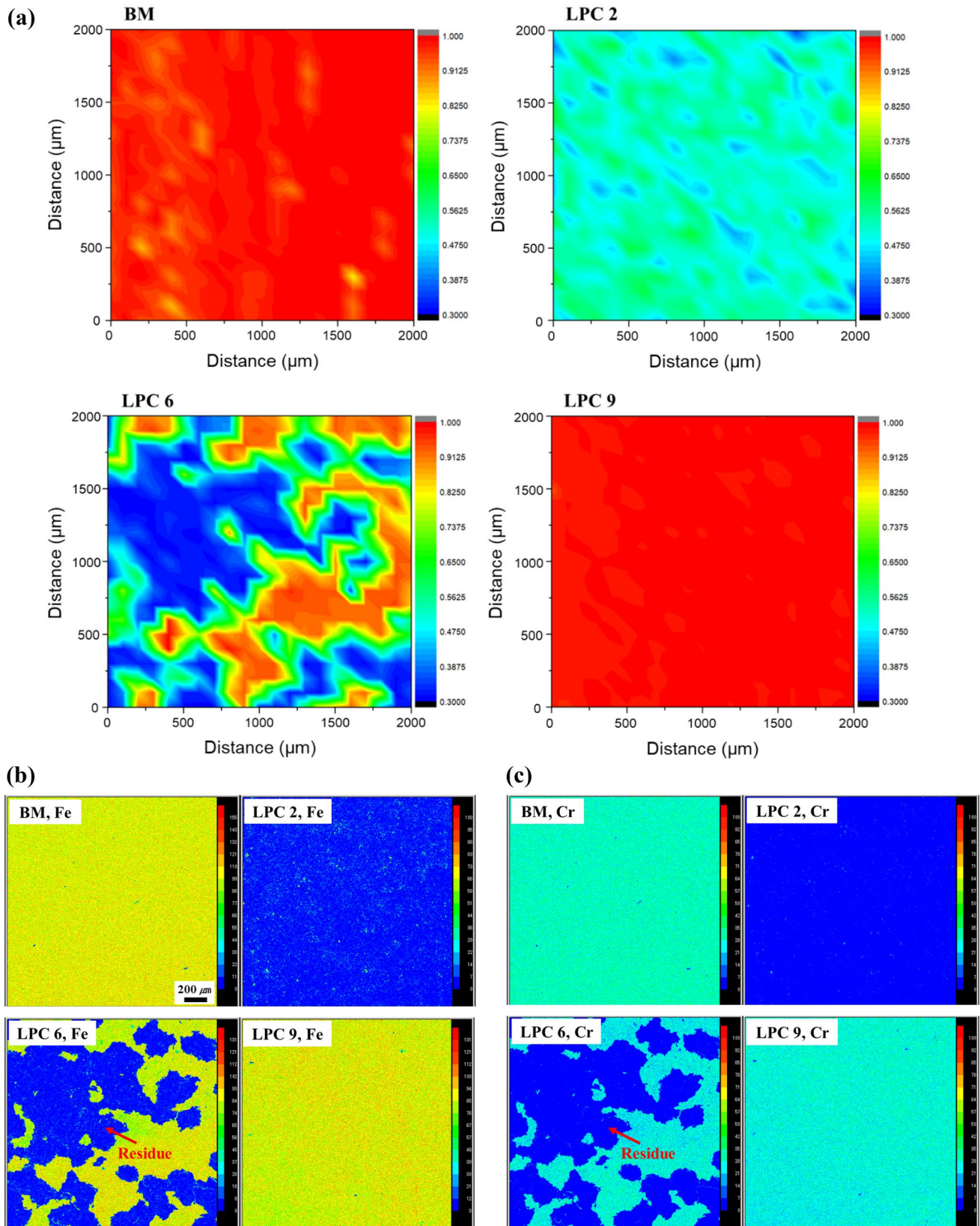


Fig. 6 LIBS-based 2D mapping of Fe, Cr, and Na elements for the **a** base metal, **b** LPC 2, **c** LPC 6, and **d** LPC 9



to those of the LPC 6. Eventually, the LIBS-based 2D elemental distribution mapping using the peak intensities of Fe, Cr, and Na is not suitable for the LPC monitoring.

3.3 LIBS-based 2D correlation coefficient mapping

To improve the accuracy of the LIBS-based LPC monitoring, multivariate correlation analysis was performed using the entire LIBS spectrum. A total of 1024 data points were acquired from the LIBS spectra of the BM and laser-cleaned specimens and used to calculate the Pearson's coefficient using Eq. (2). Four hundred Pearson's coefficients were utilized to construct each 2D mapping. Figure S3a–d show the heatmap of BM, LPC 2, LPC 6, and LPC 9 using the Pearson's coefficients, and the corresponding LIBS-based 2D correlation coefficient maps is shown in Fig. 7a. Figure 7b, c show the Fe and Cr elemental distribution maps obtained from the EPMA analysis of the BM and laser-cleaned specimens, respectively. A value of one in the Pearson's coefficient (red color in 2D mapping) indicates that the LIBS spectrum is identical to that of the BM, which indicates that paint removal is successfully achieved by the LPC process. On the other hand, smaller Pearson's coefficients (< 1) were obtained owing to the low similarity of the LIBS spectrum with that of the BM. This indicates the presence of a paint layer (or residue) at the surface owing to the poor level of the LPC process. These are expressed in light green or blue colors in the 2D mapping, depending on the level of paint removal. As shown in Fig. 7a, different 2D correlation coefficient maps were developed with or without the presence of a paint layer (or residue). Moreover, these results are in good agreement with the Fe and Cr distribution maps obtained from the EPMA analysis as shown in Fig. 7b, c, respectively. For the BM and LPC 9, the red color of the 2D maps was constructed, representing the absence of a paint layer. Relatively low Pearson's coefficients in certain regions (light red or yellow colors in 2D maps) for the BM may be attributed to surface contamination. For the LPC 2, blue and light green colors of the 2D map were developed, indicating the presence of a paint layer at the surface due to a low level of the LPC process. This result is equivalent to the cross-sectional OM image and EPMA analysis, which revealed the presence of a 200 μm paint layer at the surface. For the LPC 6, the 2D correlation coefficient distribution showed an excellent match with the elemental distribution of Fe and Cr. At the paint residue region in the Fe and Cr elemental distribution maps (Fig. 7b, c), relatively low Pearson's coefficients were obtained, resulting in a blue color distribution in the 2D correlation coefficient distribution map. In contrast, a red color distribution in the 2D correlation coefficient distribution map was developed in the laser-cleaned region owing

Table 2 Average values of the Pearson's coefficient for the BM, LPC 2, LPC 6, and LPC 9

Specimens	BM	LPC 2	LPC 6	LPC 9
Average Pearson's coefficient	0.977	0.516	0.686	0.986

to the relatively high Pearson's coefficients. This result substantiates that multivariate correlation analysis of the LIBS spectrum is an excellent approach to boost the monitoring accuracy of the LPC process. Moreover, multivariate correlation analysis is a relatively facile approach because data preparation, including background subtraction and peak intensity measurement, is not necessary.

The average values of the Pearson's coefficients for the BM, LPC 2, LPC 6, and LPC 9 are summarized in Table 1. A total of four hundred Pearson's coefficients were used to calculate the average Pearson's coefficient for each specimen. The average Pearson's coefficient increased with an increase in the number of LPC processes, and eventually, the LPC 9, where the paint layer was effectively removed by the LPC process, showed a comparable average Pearson's coefficient with that of the BM. Therefore, the average Pearson's coefficient can be used as a criterion for predicting the level of the LPC process (Table 2).

4 Conclusion

In this study, the paint removal was achieved using a high-power laser paint cleaning process. The LIBS-based monitoring was conducted to examine the SS304L surface, and two different types of LIBS-based 2D mappings were developed. The 2D elemental distribution maps of Fe, Cr, and Na with the LIBS spectrum peak intensity and the 2D correlation coefficient distribution maps by calculating the Pearson's coefficients were obtained. The 2D mappings were compared with the elemental distribution map obtained from the EPMA analysis. The multivariate analysis-based 2D correlation coefficient distribution mapping successfully distinguished between the paint residue and paint-cleaned regions. Moreover, the results were in excellent agreement with the elemental distribution map of the EPMA analysis. However, the LIBS peak intensity-based 2D elemental distribution mapping resulted in low match with that of the EPMA analysis owing to the plasma-induced LIBS signal intensity variation. This study verified the capability of multivariate analysis-based LIBS to monitor the LPC process.

Supplementary Information The online version contains supplementary material available at <https://doi.org/10.1007/s00340-022-07942-4>.

Acknowledgements This study was supported by the National Research Council of Science and Technology [Project number: NK238A, NK239D, 2022, Korea].

Author contributions SC: data curation and writing—original draft. JC: supervision. CP: supervision and writing—review and editing.

Data availability statement The data that support the findings of this study are available on request from the corresponding author.

Declarations

Competing interests The authors declare no competing interests.

Conflict of interest The authors declare no conflicts of interest.

References

- D. Yang, T.S. Khan, E. Al-Hajri, Z.H. Ayub, A.H. Ayub, Geometric optimization of shell and tube heat exchanger with interstitial twisted tapes outside the tubes applying CFD techniques. *Appl. Therm. Eng.* **152**, 559–572 (2019)
- S.J. Zinkle, G. Was, Materials challenges in nuclear energy. *Acta Mater.* **61**, 735–758 (2013)
- S. Tsouli, A. Lekatou, S. Kleftakis, T. Matikas, P. Dalla, Corrosion behavior of 304L stainless steel concrete reinforcement in acid rain using fly ash as corrosion inhibitor. *Procedia Struct. Integr.* **10**, 41–48 (2018)
- A. Marquez, A. Ramnanan, C. Maharaj, Failure analysis of carbon steel tubes in a reformed gas boiler feed water preheater. *J. Fail. Anal. Prev.* **19**, 592–597 (2019)
- D. Luder, T. Hundhausen, E. Kaminsky, Y. Shor, N. Iddan, S. Ariely, M. Yalin, Failure analysis and metallurgical transitions in SS 304L air pipe caused by local overheating. *Eng. Fail. Anal.* **59**, 292–303 (2016)
- F. Lebel, E. Abi-Aad, B. Duponchel, I.P. Serre, S. Ringot, P. Langry, A. Aboukaïs, Thermal ageing process at laboratory scale to evaluate the lifetime of liquefied natural gas storage and loading/unloading materials. *Mater. Des.* **44**, 283–290 (2013)
- J. Sanchez, O. Galao, J. Torres, J. Fullea, C. Andrade, J.C. Garcia, J. Ruesga, P. Cano, 40 years old LNG stainless steel pipeline: characterization and mechanical behavior. *Eng. Fail. Anal.* **79**, 876–888 (2017)
- B. Djurovic, E. Jean, M. Papini, P. Tangestanian, J. Spelt, Coating removal from fiber-composites and aluminum using starch media blasting. *Wear* **224**, 22–37 (1999)
- C.-K. Fang, T. Chuang, Surface morphologies and erosion rates of metallic building materials after sandblasting. *Wear* **230**, 156–164 (1999)
- A. Echt, K.H. Dunn, R.L. Mickelsen, Automated abrasive blasting equipment for use on steel structures. *Appl. Occup. Environ. Hyg.* **15**, 713–720 (2000)
- A. Raykowski, M. Hader, B. Maragno, J. Spelt, Blast cleaning of gas turbine components: deposit removal and substrate deformation. *Wear* **249**, 126–131 (2001)
- M.K.A.A. Razab, M.S. Jaafar, A.A. Rahman, S. Mamat, M.I. Ahmad, Study of health implications effects in laser paint removal process based on PM_{1.0} and PM_{10.0} measurements. *J. Trop. Resour. Sustain. Sci.* **2**, 30–39 (2014)
- S. Guo, R. Si, Q. Dai, Z. You, Y. Ma, J. Wang, A critical review of corrosion development and rust removal techniques on the structural/environmental performance of corroded steel bridges. *J. Clean. Prod.* **233**, 126–146 (2019)
- H.J. Yoo, S. Baek, J.H. Kim, J. Choi, Y.-J. Kim, C. Park, Effect of laser surface cleaning of corroded 304L stainless steel on microstructure and mechanical properties. *J. Mater. Res. Technol.* **16**, 373–385 (2022)
- G.S. Senesi, I. Allegretta, C. Porfido, O.D. Pascale, R. Terzano, Application of micro X-ray fluorescence and micro computed tomography to the study of laser cleaning efficiency on limestone monuments covered by black crusts. *Talanta* **178**, 419–425 (2018)
- P. Moretti, M. Iwanicka, K. Melessanaki, E. Dimitroulaki, O. Kokkinaki, M. Daugherty, M. Sylwestrzak, P. Pouli, P. Targowski, K.J. Berg, L. Cartechini, C. Miliani, Laser cleaning of paintings: in situ optimization of operative parameters through non-invasive assessment by optical coherence tomography (OCT), reflection FT-IR spectroscopy and laser induced fluorescence spectroscopy (LIF). *Herit. Sci.* **7**, 44 (2019)
- Z. Tian, Z. Lei, X. Chen, Y. Chen, L.C. Zhang, J. Bi, J. Liang, Nanosecond pulsed fiber laser cleaning of natural marine microbiofoulings from the surface of aluminum alloy. *J. Clean. Prod.* **244**, 118724 (2020)
- G.J. Tserevelakis, J.S. Pozo-Antonio, P. Sizos, T. Rivas, P. Pouli, G. Zacharakis, On-line photoacoustic monitoring of laser cleaning on stone: evaluation of cleaning effectiveness and detection of potential damage to the substrate. *J. Cult. Herit.* **35**, 108–115 (2019)
- X. Xiea, Q. Huang, J. Long, Q. Ren, W. Hu, S. Liu, A new monitoring method for metal rust removal states in pulsed laser derusting via acoustic emission techniques. *J. Mater. Process. Technol.* **275**, 116321 (2020)
- A. Papanikolaou, G.J. Tserevelakis, K. Melessanaki, C. Fotakis, G. Zacharakis, P. Pouli, Development of a hybrid photoacoustic and optical monitoring system for the study of laser ablation processes upon the removal of encrustation from stonework. *Opto-Electron. Adv.* **3**, 190037 (2020)
- W. Zou, F. Song, Y. Luo, Characteristics of audible acoustic signal in the process of laser cleaning of paint on metal surface. *Opt. Laser Technol.* **144**, 107388 (2021)
- F. Colao, R. Fantoni, V. Lazic, A. Morone, A. Santagata, A. Giardini, LIBS used as a diagnostic tool during the laser cleaning of ancient marble from Mediterranean areas. *Appl. Phys. A* **79**, 213–219 (2004)
- A. Staicu, I. Apostol, A. Pascu, I. Urzica, M.L. Pascu, V. Damian, Minimal invasive control of paintings cleaning by LIBS. *Opt. Laser Technol.* **77**, 187–192 (2016)
- J.H. Scholten, J.M. Teule, V. Zafropoulos, R.M.A. Heeren, Controlled laser cleaning of painted artworks using accurate beam manipulation and on-line LIBS-detection. *J. Cult. Herit.* **1**, S215–S220 (2000)
- R. Salimbeni, R. Pini, S. Siano, Achievement of optimum laser cleaning in the restoration of artworks: expected improvements by on-line optical diagnostics. *Spectrochim. Acta B* **56**, 877–885 (2001)
- G.S. Senesi, I. Carrara, G. Nicolodelli, D.M.B.P. Milori, O.D. Pascale, Laser cleaning and laser-induced breakdown spectroscopy applied in removing and characterizing black crusts from limestones of Castello Svevo, Bari, Italy: a case study. *Microchem. J.* **124**, 296–305 (2016)
- F. Colao, R. Fantoni, V. Lazic, L. Caneve, A. Giardini, V. Spizichino, LIBS as a diagnostic tool during the laser cleaning of copper based alloys: experimental results. *J. Anal. At. Spectrom.* **19**, 502–504 (2004)
- M. Kono, K.G.H. Baldwin, A. Wain, A.V. Rode, Treating the untreatable in art and heritage materials: ultrafast laser cleaning of “cloth-of-gold.” *Langmuir* **31**, 1596–1604 (2015)
- F.J. Fortes, L.M. Cabalín, J.J. Laserna, The potential of laser-induced breakdown spectrometry for real time monitoring the

- laser cleaning of archaeometallurgical objects. *Spectrochim. Acta B* **63**, 1191–1197 (2008)
30. S. Marimuthu, S. Pathak, J. Radhakrishnan, A.M. Kamara, In-process monitoring of laser surface modification. *Coatings* **11**, 886 (2021)
 31. X. Li, Y. Guan, Real-time monitoring of laser cleaning for hot-rolled stainless steel by laser-induced breakdown spectroscopy. *Metals* **11**, 790 (2021)
 32. M.P. Mateo, V. Piñon, G. Nicolas, Vessel protective coating characterization by laser-induced plasma spectroscopy for quality control purposes. *Surf. Coat.* **211**, 89–92 (2012)
 33. S. Kheiri, H. Mirzadeh, M. Naghizadeh, Tailoring the microstructure and mechanical properties of AISI 316L austenitic stainless steel via cold rolling and reversion annealing. *Mater. Sci. Eng. A* **759**, 90–96 (2019)
 34. W. Rapin, B. Bousquet, J. Lasue, P.Y. Meslin, J.L. Lacour, C. Fabre, R.C. Wiens, J. Frydenvang, E. Dehouck, S. Maurice, O. Gasnault, O. Forni, A. Cousin, Roughness effects on the hydrogen signal in laser-induced breakdown spectroscopy. *Spectrochim. Acta B* **137**, 13–22 (2017)
 35. C. Song, X. Gao, Y. Shao, Pre-ablation laser parameter effects on the spectral enhancement of 1064 nm/1064 nm dual-pulse laser induced breakdown spectroscopy. *Optik* **127**, 3979–3983 (2016)
 36. K.L. Eland, D.N. Stratis, D.M. Gold, S.R. Goode, S.M. Angel, Energy dependence of emission intensity and temperature in a LIBS plasma using femtosecond excitation. *Appl. Spectrosc.* **55**, 286–291 (2001)
 37. A.J. Effenberger, J.R. Scott, Effect of atmospheric conditions on LIBS spectra. *Sensors* **10**, 4907–4925 (2010)
 38. A. Williams, K. Bryce, S. Phongikaroon, Measurement of cerium and gadolinium in solid lithium chloride-potassium chloride salt using laser-induced breakdown spectroscopy (LIBS). *Appl. Spectrosc.* **71**, 2302–2312 (2017)

Publisher's Note Springer Nature remains neutral with regard to jurisdictional claims in published maps and institutional affiliations.

Springer Nature or its licensor (e.g. a society or other partner) holds exclusive rights to this article under a publishing agreement with the author(s) or other rightsholder(s); author self-archiving of the accepted manuscript version of this article is solely governed by the terms of such publishing agreement and applicable law.